



HAL
open science

Non-cooperative low-complexity detection approach for FHSS-GFSK drone control signals

Dan Mototolea, Roua Youssef, Emanuel Radoi, Ioan Nicolaescu

► To cite this version:

Dan Mototolea, Roua Youssef, Emanuel Radoi, Ioan Nicolaescu. Non-cooperative low-complexity detection approach for FHSS-GFSK drone control signals. *IEEE Open Journal of the Communications Society*, 2020, 1 (1), pp.401-412. 10.1109/OJCOMS.2020.2984312 . hal-02531763

HAL Id: hal-02531763

<https://hal.science/hal-02531763v1>

Submitted on 29 Sep 2024

HAL is a multi-disciplinary open access archive for the deposit and dissemination of scientific research documents, whether they are published or not. The documents may come from teaching and research institutions in France or abroad, or from public or private research centers.

L'archive ouverte pluridisciplinaire **HAL**, est destinée au dépôt et à la diffusion de documents scientifiques de niveau recherche, publiés ou non, émanant des établissements d'enseignement et de recherche français ou étrangers, des laboratoires publics ou privés.



Distributed under a Creative Commons Attribution 4.0 International License

Non-Cooperative Low-Complexity Detection Approach for FHSS-GFSK Drone Control Signals

DAN MOTOTOLEA¹, ROUA YOUSSEF² (Member, IEEE), EMANUEL RADOI² (Senior Member, IEEE), AND IOAN NICOLAESCU¹ (Member, IEEE)

¹Department of Communications and Military Electronic Systems, Military Technical Academy, 050141 Bucharest, Romania

²Lab-STICC, CNRS, UMR 6285, Université de Bretagne Occidentale, 29200 Brest, France

CORRESPONDING AUTHOR: E. RADOI (e-mail: radoi@univ-brest.fr)

This work was supported by the Fonds Européen de Développement Régional Project ANDRO under Grant 19004705.

ABSTRACT The commercial drone market has substantially grown over the past few years. While providing numerous advantages in various fields and applications, drones also provide ample opportunities for misuse by irresponsible hobbyists or malevolent actors. The increasing number of safety/security incidents in which drones are involved has motivated researchers to find new and ingenious ways to detect, locate and counter this type of vehicles. In this paper, we propose a new method to detect frequency hopping spread spectrum - Gaussian frequency-shift keying (FHSS-GFSK) drone communication signals, in a non-cooperative scenario, where no prior information about the signals of interest is available. The system is designed to detect and retrieve data bit sequences through a compressive sampling approach, which includes the extraction of the reduced spectral information and a soft detection algorithm. The performance of the proposed approach is assessed in terms of bit error rate and compared with that of a Viterbi detector and a neural network-based detector. The effectiveness of the method described in the paper highlights the fact that current UAV communications are not infallible and present real security issues.

INDEX TERMS Counter-drone measures, FHSS-GFSK communication signals, non-cooperative data detection, compressive sampling, security of UAV communications.

I. INTRODUCTION

UNMANNED aerial vehicles (UAVs), commonly known as drones, are readily available and easy to use. Drones are no longer only related to military applications but also to services that can offer huge potential for developing innovative civil applications in a wide variety of sectors, including filming and entertainment, transportation, mapping, prospecting, data collection and analytics, environmental and wild life monitoring. The rapid growth of the drone market in the past few years has increased the number of unintentionally and intentionally safety and security violations in which drones are involved [1]. According to [2] the global drone market is expected to grow from \$14 billion in 2018 to over \$43 billion by 2024 at a compound annual growth rate of 20.5%. The growing number

of incidents that appear almost daily in the media has prompted an increase in the research of surveillance and interdiction methods tailored for drones. Different drone detection systems have been recently developed, based on the following physical effects and corresponding sensors [3]: reflectance of UV/visible/NIR/SWIR/MWIR/LWIR photons [4], [5], radar reflectance [6], [7], [8], acoustic emissions [9], [10], electromagnetic emissions from onboard radios [11], [12], or other communication links. Each sensor has its own limitations and can be used under some specific conditions. Since none of them can provide full protection against drones, different sensors may be combined in order to increase the detection rate. The method described in this paper belongs to the category of RF eavesdroppers [13].

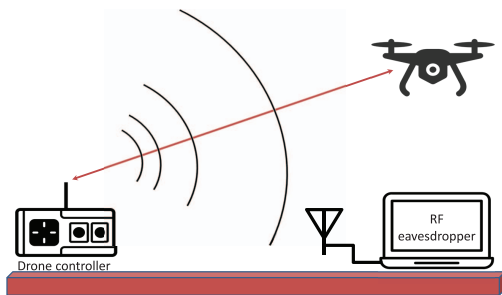


FIGURE 1. Application framework illustration: detection of drone control signals by an RF eavesdropper.

We consider the non-cooperative scenario presented in Fig. 1, with the detection system acting as an eavesdropper. The objective is to detect the signal transmitted by the drone controller and to recover the underlying data bit sequences, as the first step toward effective counter-drone measures, such as taking control of the drone or smart jamming the communication between this one and its controller. Therefore, the proposed approach can be helpful in detecting the use or intrusions of drones in perimeters in which their flight is prohibited.

Four types of wireless communication technologies are used to control drones [14, Table 3]: point-to-point (direct link) communications, satellite communications, ad-hoc network communications and cellular network communications. The method described in this paper is applicable to point-to-point (controller-drone) communications, which is the most widely used for commercial UAVs. Although cellular networks offer drone command and control capabilities, this type of communication is not yet widespread because regulations in most countries limit the flight of UAV to the visual line of sight of a human pilot, who is constantly controlling the drone. For consumer-grade drones, no specific frequency allocations have been made yet at international level. Therefore, in most countries, drones only use the license-free spectrum. The communication between the drone and its controller is covered by the IEEE 802.11 family of LAN protocols [15]. Three standard links are commonly associated with the UAV: the control link, telemetry link and video link. The 2.4 and the 5.8 GHz bands are the most often used for transmitting the control and video information respectively. The telemetry link is usually sent overlaid the video link, or in the radio channels corresponding to the 868 MHz, 433 MHz or 2.4 GHz frequency bands. According to [16] and [17, p. 35], drone controllers usually operate in the 2.4 GHz band, the carrier frequency being randomly changed for each data bit sequence using the frequency hopping spread spectrum (FHSS) technique [18]. FHSS is used for making the communication secure and resistant to eavesdropping and interferences from other signals. Within a data sequence, the data bits are usually coded using Gaussian frequency shift keying (GFSK) [19], due to its power and spectral efficiencies, which are among

the most important performance criteria for modulation schemes.

The promising drone market has recently increased the interest in UAV security issues, including current and future wireless networks. Communications security can be addressed either at the upper layers of the communication protocol, through operations such as encryption/decryption, or at the physical layer level, by exploiting the intrinsic characteristics of wireless channels [20]. A survey on this topic is presented in [21], where several security issues are identified from the physical layer point of view. The safeguarding of wireless networks is discussed in [22] from the same perspective, while the main security aspects of wireless sensor networks against jamming attacks are reviewed in [23]. Several other papers and magazine surveys raised awareness related to the safeguarding of UAV communications. Thus, since FHSS has been the most widely used technique to date, for ensuring the security of the physical layer [22], a method is introduced in [24] to extract the hopping sequences from FHSS-type UAV controllers, and its effectiveness is demonstrated using software defined radio. A technique for tracking frequency hopping patterns and frequency components over time is also presented in [25], while a versatile system with protocol-aware jamming capabilities against different UAV remote control systems is described in [26]. Our work contributes to assessing the extent to which current communications are secure to support large-scale UAV services. However, unlike most previous research, which focuses on different aspects related to FHSS communications jamming [23], [26], [27], our paper proposes an approach to detect the FHSS-GFSK signals and recover the transmitted data bit sequences by eavesdropping on the communication between the UAV and its controller.

Throughout the paper it is assumed that during each randomly chosen frequency hop, the drone controller transmits on one of the N_c frequency sub-channels in the 2.4-2.48 GHz band, each channel having bandwidth B . In a non-cooperative scenario, the drone detector does not know which sub-channel is being used during each frequency hop, so its Nyquist sampling rate is $2N_cB$, instead of $2B$. However, as the signal is sparse in the frequency domain, a compressive sampling (CS) approach [28] can be used for the detection process, resulting in good detection performance at sampling rates much lower than the Nyquist limit. Many studies and research works on this topic have been performed since the introduction of CS in 2004 by Donoho, Candès, Romberg, and Tao [29], [30], [31]. Thus, a method for detecting wideband FH signals with a tiny number of incoherent measurements is presented in [32], whereas different methods for detecting FHSS signals from compressive measurements are proposed in [33] and [34]. Finally, a closely related research work [35], which is considered a reference throughout this paper, relies on a Viterbi sequence detector (VD) to recover the transmitted bits from compressively sampled FHSS-GFSK signals.

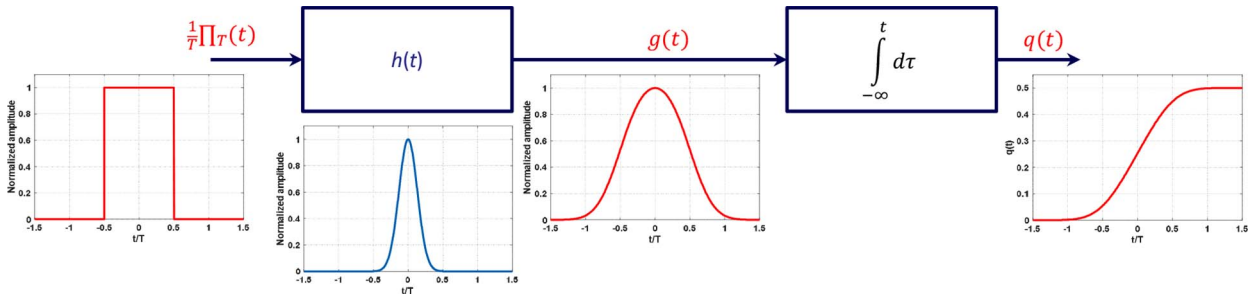


FIGURE 2. Illustration of the phase term $q(t)$ generation for $BT = 0.5$.

The original contributions of this paper can be summarized as follows. Compared with the related research papers cited above, the proposed approach skips the signal reconstruction phase, and aims at directly detecting the sequences of bits transmitted by the drone controller. We maintain the idea of the CS-based scheme to digitalize the received signal, but unlike the approach proposed in [35], the data bit sequences are recovered using the signal spectral representation, instead of its temporal one. In fact, only a small part of the signal spectrum, called reduced spectral information (RSI), is reconstructed using the orthogonal matching pursuit (OMP) algorithm [36]. To the best of our knowledge, this detection approach is original and has never been proposed so far. Another important contribution of the paper is a new highly effective 2D feature vector, which is calculated from the OMP-reconstructed RSI and does not depend on the initial phase of the received signal. Hence, its estimation is no longer necessary, which reduces the detection method complexity. The proposed feature vector also has little sensitivity to the GFSK modulation index, which makes the detection method more tolerant to its estimation errors. The efficiency of the proposed method is further increased by a soft-detection (SD) algorithm using confidence coefficients instead of a hard threshold. Lastly, the complexity of the new detection method is lower than that corresponding to the reference Viterbi algorithm for compressively sampled signals. Of note, the application of the proposed approach is not limited to the detection of drone control signals. Actually, it can be easily adapted for detecting any FHSS-GFSK signals, such as Bluetooth signals.

The remainder of this paper is organized as follows. The FHSS-GFSK signal model and the main idea of the proposed approach are introduced in Section II. The new detection method is then thoroughly explained in Section III. We describe the extraction of the RSI, the soft detection of the data sequence, and the global processing flowchart. The simulation results are provided in Section IV. The performance of the proposed approach, in terms of bit error rate (BER), is compared with that of a Viterbi detector and a multilayer perceptron (MLP) neural network-based detector. We demonstrate that our method is appropriate for low-complexity non-cooperative detection of drone control signals, as it requires low sampling frequencies and does

not need initial-phase. Finally, some conclusions are drawn in Section V, and different research paths are proposed as future works.

II. SIGNAL MODEL AND MAIN IDEA OF THE PROPOSED DETECTION METHOD

As stated above, we consider in this paper an FHSS-GFSK drone control signal, which employs frequency hopping for spreading the spectrum and GFSK modulation at each frequency hop. N_s data bits $\{d_n = \pm 1\}_{n=0, \dots, N_s-1}$ are transmitted during a frequency hop, on a subcarrier frequency f_c randomly chosen over N_c subchannels of central frequencies $\{f_k\}_{k=1, \dots, N_c}$ and bandwidth B . The analytic signal corresponding to the time interval $[(n-1)T, nT]$ is given below:

$$x_n(t) = A e^{j[2\pi f_c + 2\pi h \sum_{i=0}^n d_i q(t-iT) + \varphi_0]}, \quad n = 1, \dots, N_s - 1, \quad (1)$$

where h is the GFSK modulation index, and A and φ_0 stand for the signal amplitude and its initial random phase associated to f_c , respectively.

Function $q(t) = \int_{-\infty}^t g(\tau) d\tau$ is obtained by integrating $g(t) = \frac{1}{2T} \{F[\gamma B(t+T/2)] - F[\gamma B(t-T/2)]\}$, as illustrated in Fig. 2 for $BT = 0.5$, where $F(x)$ is the normalized Gaussian cumulative distribution function and $\gamma = \frac{2\pi}{\sqrt{\ln 2}}$.

As shown in Fig. 2, function $q(t)$ can be considered zero for $t < -T$ and equal to 1 for $t > T$. Consequently, $q(t-iT) = 1/2$ for $i = 0, \dots, n-2$, so the signal specific phase term from Eq. (1) can be rewritten as follows:

$$2\pi h \left(0.5 \sum_{i=0}^{n-2} d_i + d_{n-1} q(t - (n-1)T) + d_n q(t - nT) \right) = \varphi_n + \theta(t - nT), \quad (2)$$

where $\varphi_n = \pi h \sum_{i=0}^{n-2} d_i$, $n = 2, \dots, N_s - 1$ is a cumulative phase term, which is constant during the $[(n-1)T, nT]$ time interval, and $\theta(t) = 2\pi h (d_{n-1} q(t+T) + d_n q(t))$ is a time-variant phase term depending only on the couple of bits $\{d_{n-1}, d_n\}$. For the sake of simplicity, we use throughout the paper the notation $\theta(t)$ for a generic couple of bits $\{d_{n-1}, d_n\}$ and $\{\theta_i(t)\}_{i=1, \dots, 4}$ for the specific combinations: $\{d_{n-1} = 1, d_n = 1\}$, $\{d_{n-1} = -1, d_n = -1\}$, $\{d_{n-1} = 1, d_n = -1\}$ and $\{d_{n-1} = -1, d_n = 1\}$.

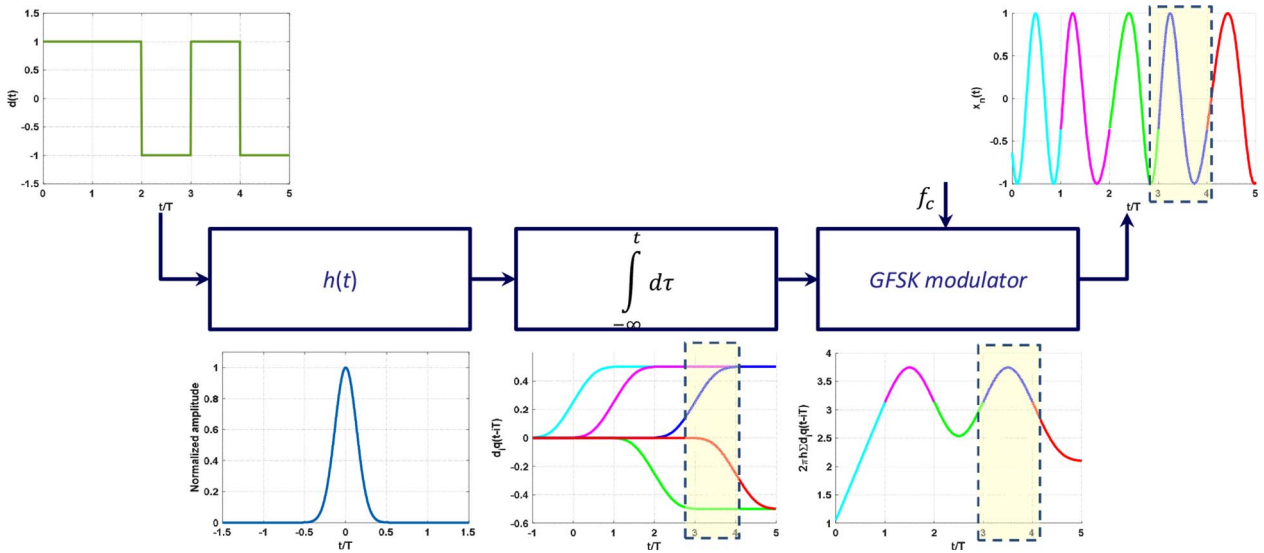


FIGURE 3. Illustration of the signal generation, for the data bit sequence $\{d_0 = 1, d_1 = 1, d_2 = -1, d_3 = 1, d_4 = -1\}$ and modulation index $h = 1/3$.

The real signal generation is illustrated in Fig. 3 for the data bit sequence $\{d_0 = 1, d_1 = 1, d_2 = -1, d_3 = 1, d_4 = -1\}$. Thus, for example, signal $x_4(t)$ is defined on the time interval $[3T, 4T]$ and the specific phase term equals $\varphi_4 + \theta(t - 4T) = \pi h \sum_{i=0}^2 d_i + 2\pi h(d_3 q(t - 3T) + d_4 q(t - 4T))$.

The detection method proposed in this paper relies on the following key remarks. From Eq. (1) and (2) it can be concluded that considering known $\{f_c, \varphi_0\}$ and an iterative detection process, i.e., already detected previous data bits $\{d_i\}_{i=0, \dots, n-1}$, signal $x_n(t)$ only depends on $\theta(t)$ or equivalently on the couple $\{d_{n-1}, d_n\}$. The main idea of the approach described in [35] is that as signal $x_n(t)$ can be completely characterized by these elements, a VD can be used to recover the data bit sequences. Thus, at each stage of the iterative detection process, the most likely couple $\{d_{n-1}, d_n\}$ can be determined using a trellis diagram, with known φ_0 and estimated φ_n from the previously detected bits $\{d_i\}_{i=0, \dots, n-2}$. The estimation of the current FHSS subcarrier frequency f_c is also integrated into the detection process, because a trellis diagram is considered for each one of the N_c subchannels. To avoid the reconstruction of signal $x_n(t)$, the Viterbi detection process is associated with a CS scheme (VD&CS), which results in a significant reduction of the sampling frequency compared with the Nyquist limit.

In this paper we maintain the idea of the CS to digitalize the received signal, which is the input of the signal processing flow. However, we propose a completely different approach for the detection of the data bit sequence, which represents its output. Thus, as it will be explained in the next section, unlike the approach addressed in [35], the couple of data bits $\{d_{n-1}, d_n\}$ is estimated using the signal $x_n(t)$ spectral representation, instead of its temporal one. On the basis of the signal sparsity in the frequency domain, a small but salient part of its spectrum, called RSI, is reconstructed using the OMP algorithm. Then, a highly discriminant 2D feature vector is extracted from the RSI for estimating the

most likely couple $\{d_{n-1}, d_n\}$ among the four possible bits combinations.

III. DETECTION APPROACH BASED ON RSI

We consider the spectral representation of signal $x_n(t)$:

$$\begin{aligned} X_n(\nu) &= \int_{-\infty}^{\infty} e^{j[2\pi f_c t + \theta_n(t) + \varphi_n + \varphi_0]} e^{-j2\pi \nu t} dt \\ &= e^{j(\varphi_n + \varphi_0)} \int_{-\infty}^{\infty} e^{j\theta(t-nT)} e^{-j2\pi(\nu - f_c)t} dt \\ &= e^{j(\varphi_n + \varphi_0)} \Theta(\nu - f_c) e^{-j2\pi nT(\nu - f_c)}, \end{aligned} \quad (3)$$

where $\Theta(\nu)$ is the Fourier transform of signal $e^{j\theta(t)}$. As $\Theta(\nu)$ cannot be calculated in closed-form, the graphical representation of its amplitude is given in Fig. 4 for $\{d_{n-1} = 1, d_n = -1\}$ and $\{d_{n-1} = 1, d_n = 1\}$. The first representation is also obtained for $\{d_{n-1} = -1, d_n = 1\}$ and the frequency-reversed second representation for $\{d_{n-1} = -1, d_n = -1\}$.

These representations are obtained from signal $x_n(t)$ sampled at the Nyquist rate $F_{\text{Nyq}} = 2N_c B$. The N_T -points FFT is then calculated, with $N_T = 2N_c$, which means that the spectral components are equally spaced by $1/T$. As clearly shown in these representations, the FHSS subcarrier frequency can be easily estimated by seeking the maximum of $|X_n(\nu)| = |\Theta(\nu - f_c)|$ as illustrated in Fig. 5. Moreover, the signal is relatively sparse in the frequency domain, so its spectrum can be reconstructed using the OMP algorithm. As shown in the next section, only the useful information, represented by the strongest spectral component and the two adjacent ones, is extracted.

A. RSI EXTRACTION

We consider the CS scheme defined in [35], with L sampling branches and collecting M samples per symbol. Then, using

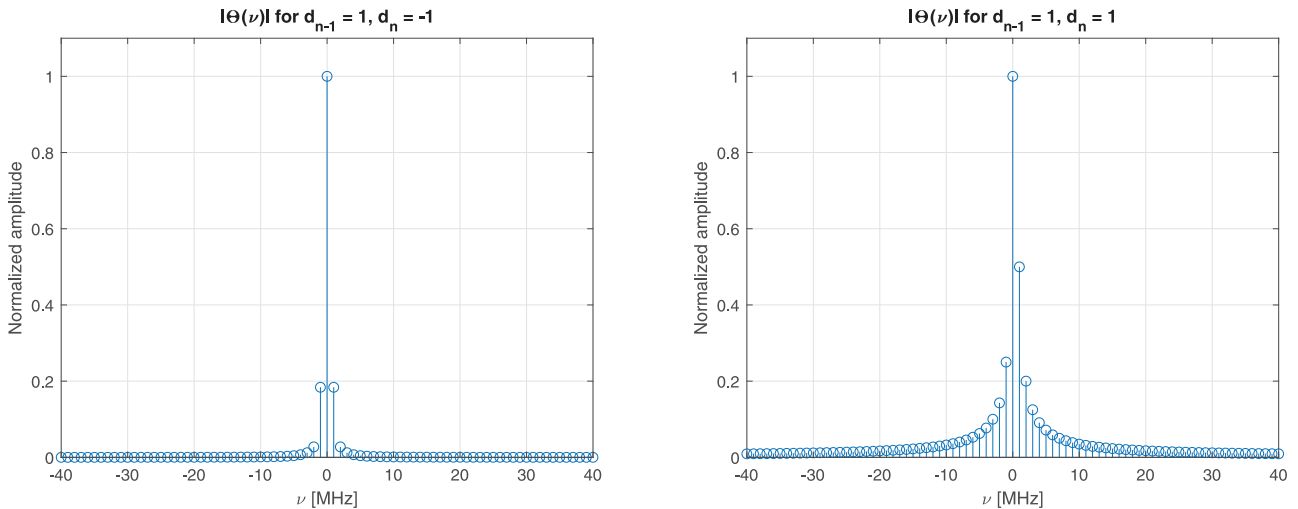


FIGURE 4. Graphical representation of amplitude spectrum $|\Theta(\nu)|$ for different couples of data bits (d_{n-1}, d_n) .

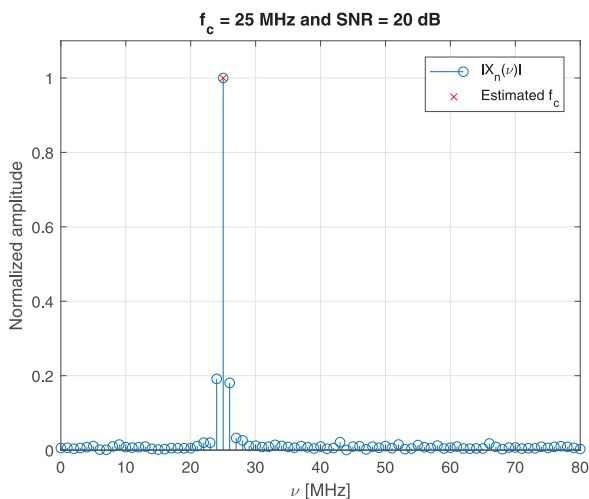


FIGURE 5. FHSS subcarrier frequency estimation from the amplitude spectrum $|X_n(\nu)|$.

the same notations, the measurement vector at the output of this scheme, for time interval $[(n-1)T, nT]$, is defined by

$$\mathbf{y}_n = \mathbf{A}\mathbf{x}_n = \mathbf{A}\mathbf{E}^*\mathbf{X}_n = \mathbf{W}\mathbf{X}_n, \quad (4)$$

where \mathbf{x}_n and \mathbf{X}_n are the $N_T \times 1$ vectors corresponding to the Nyquist sampled signal and its discrete spectrum respectively, \mathbf{A} is the $LM \times N_T$ measurement matrix defined in [35, p. 5968], $\mathbf{E} = \{e^{-j2\pi kp/N_T}\}_{k=0, \dots, N_T-1, p=0, \dots, N_T-1}$ is the $N_T \times N_T$ DFT matrix, and $\mathbf{W} = \mathbf{A}\mathbf{E}^*$.

Compared with the Nyquist sampling, the number of samples is reduced for the CS scheme with the compression factor $CR = N_T/(LM) = 2N_c/(LM)$. Moreover, the sampling frequency on each one of the L sampling branches is $f_b = M/T$, i.e., $2N_c/M$ times lower than the Nyquist frequency.

OMP is a greedy algorithm [36], widely used for finding the sparse solution $\hat{\mathbf{X}}_n$ of the problem described by Eq. (4):

$$\hat{\mathbf{X}}_n = \arg \min_{\mathbf{X}_n} \|\mathbf{y}_n - \mathbf{W}\mathbf{X}_n\|_2^2 \quad \text{subject to } \|\mathbf{X}_n\|_0 \leq s, \quad (5)$$

where s denotes the sparsity order of \mathbf{X}_n .

In this paper a simplified version of OMP is considered, as the RSI consists of three consecutive components of the sparse spectrum \mathbf{X}_n . The strongest one, corresponding to the carrier frequency f_c , is firstly detected by searching the column of the matrix \mathbf{W} that is the most correlated with input vector \mathbf{y}_n :

$$i_{\text{opt}} = \arg \max_{l=1, \dots, N_T} \frac{|\langle \mathbf{y}_n, \mathbf{w}_l \rangle|}{\|\mathbf{y}_n\| \|\mathbf{w}_l\|}. \quad (6)$$

The localization of the three spectral components is then defined by vector $\mathbf{i}_n = [i_{\text{opt}} - 1, i_{\text{opt}}, i_{\text{opt}} + 1]$. We denote by $\hat{\mathbf{X}}_n = \hat{\mathbf{X}}_n(\mathbf{i}_n)$ the solution vector reduced to its non-zero components and by $\underline{\mathbf{W}} = \mathbf{W}(:, \mathbf{i}_n)$ the matrix formed with the columns of \mathbf{W} corresponding to vector \mathbf{i}_n elements. Reference [36] shows that:

$$\min_{\mathbf{X}_n} \|\mathbf{y}_n - \mathbf{W}\mathbf{X}_n\|_2^2 = \min_{\underline{\mathbf{X}}_n} \|\mathbf{y}_n - \underline{\mathbf{W}}\underline{\mathbf{X}}_n\|_2^2. \quad (7)$$

The advantage of this equivalent form is that, unlike the initial problem, it results in a unique solution:

$$\hat{\underline{\mathbf{X}}}_n = \underline{\mathbf{W}}^\dagger \mathbf{y}_n, \quad (8)$$

where $\underline{\mathbf{W}}^\dagger$ is the Moore-Penrose pseudo-inverse of $\underline{\mathbf{W}}$. The estimation of subcarrier frequency f_c and the extraction of the RSI using OMP are summarized in Algorithm 1.

The RSI extraction using the OMP algorithm is illustrated in Fig. 6, for $f_c = 25$ MHz, $\{d_{n-1} = 1, d_n = -1\}$, and two SNR values (20 and 0 dB). the subcarrier frequency is perfectly estimated in both cases and the RSI extracted with the OMP algorithm and FFT is closely related.

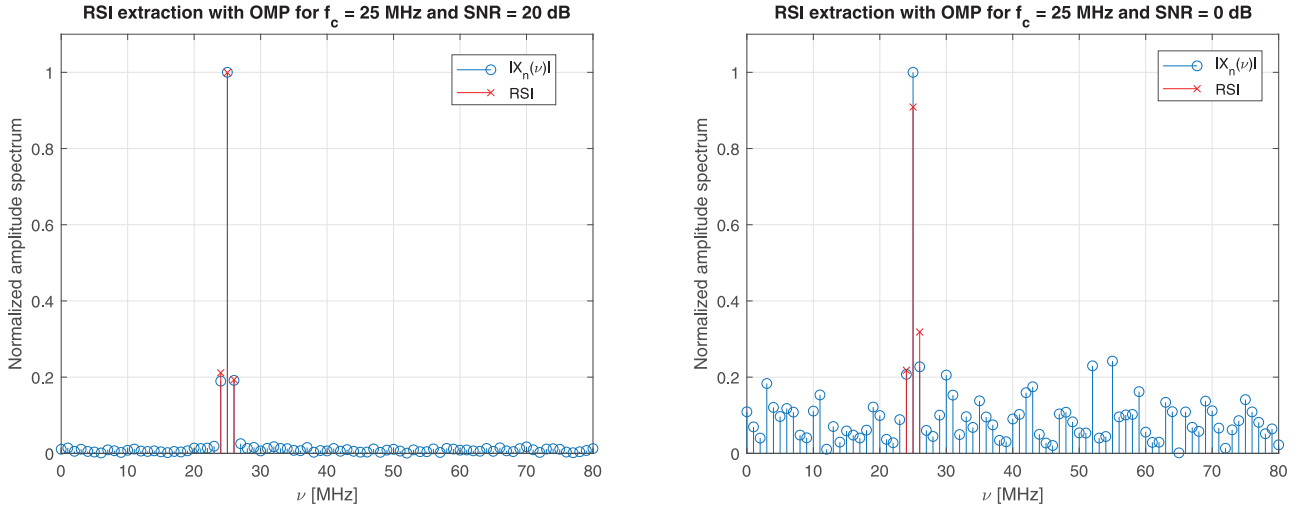


FIGURE 6. Illustration of the RSI extraction using the OMP algorithm.

Algorithm 1 Subcarrier Frequency Estimation and Extraction of the RSI.

Input: $LM \times 1$ vector \mathbf{y}_n at the output of the CS scheme;

$LM \times N_T$ matrix $\mathbf{W} = \mathbf{A}\mathbf{E}^*$.

Output: Vector $\hat{\mathbf{X}}_n$ containing the RSI; subcarrier frequency estimate \hat{f}_c .

- 1: Search $i_{\text{opt}} = \arg \max_{l=1, \dots, N_T} \frac{|\langle \mathbf{y}_n, \mathbf{w}_l \rangle|}{\|\mathbf{y}_n\| \|\mathbf{w}_l\|}$.
 - 2: Set $\mathbf{i}_n = [i_{\text{opt}} - 1, i_{\text{opt}}, i_{\text{opt}} + 1]$.
 - 3: Set $\mathbf{W} = \mathbf{W}(:, \mathbf{i}_n)$.
 - 4: Calculate $\hat{\mathbf{X}}_n = \mathbf{W}^\dagger \mathbf{y}_n$, and $\hat{f}_c = i_{\text{opt}}/T$.
-

B. DATA SEQUENCE DETECTION

In the previous section, we determined the RSI, which is theoretically given in the noiseless case by $\mathbf{X}_n = [c_{-1}^{(n)} c_0^{(n)} c_1^{(n)}]^T$, with $c_k^{(n)}$ calculated in accordance with Eq. (3):

$$\begin{aligned} c_k^{(n)} &= X_n(f_c + k/T) = e^{j(\varphi_n + \varphi_0)} \Theta(k/T) e^{-j2\pi nk} \\ &= e^{j(\varphi_n + \varphi_0)} e^{j\psi_k} |\Theta(k/T)|, \end{aligned} \quad (9)$$

where $\psi_k = \arg\{\Theta(k/T)\}$.

We define the following feature vector, which does not depend on φ_0 or φ_n :

$$\mathbf{p}^{(n)} = \begin{bmatrix} p_1^{(n)} \\ p_2^{(n)} \end{bmatrix} = \begin{bmatrix} \cos\left(\arg\{\hat{c}_0^{(n)}\} - \arg\{\hat{c}_{-1}^{(n)}\}\right) \\ \sin\left(\arg\{\hat{c}_0^{(n)}\} - \arg\{\hat{c}_1^{(n)}\}\right) \end{bmatrix}, \quad (10)$$

Indeed, in the noiseless case the feature vector becomes $\mathbf{p}^{(n)} = [\cos(\psi_0 - \psi_{-1}) \quad \sin(\psi_0 - \psi_1)]^T$ and therefore depends only on phases $\{\psi_{-1}, \psi_0, \psi_1\}$. We denote the four corresponding ideal feature vectors by $\{\mathbf{P}_i\}_{i=1, \dots, 4}$. As the Fourier transform $\Theta(\nu)$ is mathematically intractable, phases $\{\psi_{-1}, \psi_0, \psi_1\}$ are numerically calculated for each one of the four possible couples $\{d_{n-1}, d_n\}$. Nevertheless, a piecewise linear approximation of function $q(t)$ is employed in the Appendix to derive a comparable closed form of the

feature vector defined above and to better explain its discriminant capability and weak sensitivity to the modulation index variation.

Feature vectors $\mathbf{p}^{(n)}$, obtained for 360 uniformly distributed values of φ_0 between 0 and 2π , for all the subcarrier frequencies, and for a random data sequence with $N_s = 650$, are plotted in Fig. 7, for an SNR of 10 dB. The couples of values $(L = 4, M = 40)$ and $(L = 4, M = 10)$ are considered, resulting in compression ratios $CR = 1$ and $CR = 4$ respectively. The findings show that the two features are a good choice to discriminate the four combinations of $\{d_{n-1}, d_n\}$. Moreover, for each class, the feature vectors are distributed inside the unit square, around centroids $\{\mathbf{P}_i\}_{i=1, \dots, 4}$.

The detection performance can be even further improved if we take into account that each data bit d_n is estimated twice from $x_n(t)$ and $x_{n+1}(t)$, respectively. Consequently, we introduce a decision confidence coefficient to select the most likely estimation \hat{d}_n :

$$\mu^{(n)} = 1 - \frac{4 \min_{i=1, \dots, 4} \text{dist}\{\mathbf{p}^{(n)}, \mathbf{P}_i\}}{\sum_{i=1}^4 \text{dist}\{\mathbf{p}^{(n)}, \mathbf{P}_i\}} \quad (11)$$

where $\text{dist}\{\mathbf{p}^{(n)}, \mathbf{P}_i\}$ is the Euclidean distance between $\mathbf{p}^{(n)}$ and \mathbf{P}_i . Thus, when vector $\mathbf{p}^{(n)}$ is the same as one of the four centroids \mathbf{P}_k , the confidence coefficient is equal to 1. In another sense, it becomes 0 when vector $\mathbf{p}^{(n)}$ is equally spaced from centroids \mathbf{P}_i . This approach can be termed as ‘‘soft detection’’, because the decision is not made in accordance with a hard threshold but relies on confidence coefficients, with values between 0 and 1. The data sequence SD process can then be summarized in Algorithm 2 presented below.

C. PROCESSING FLOWCHART OF THE DETECTION APPROACH

The processing flowchart of the proposed approach for the detection of drone control signals is shown in Fig. 8. The

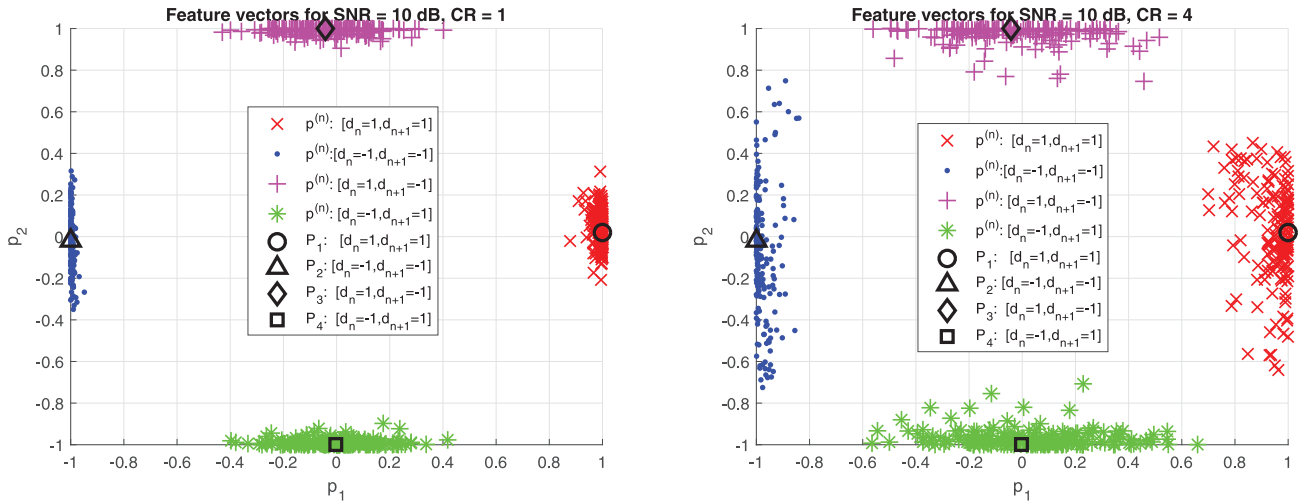


FIGURE 7. Distribution of feature vectors $\mathbf{p}^{(n)}$ calculated from the OMP-extracted RSI.

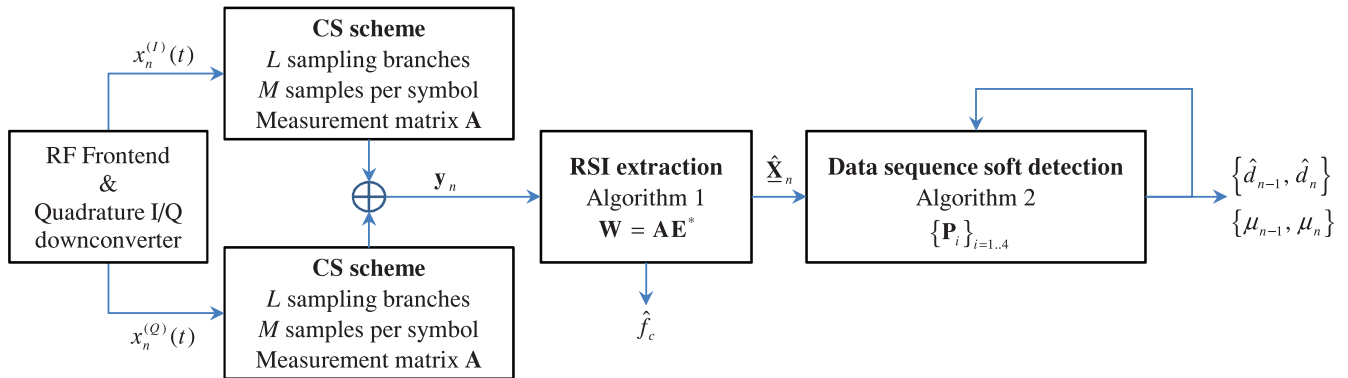


FIGURE 8. Processing flowchart of the RSI-based SD.

received signal is first frequency shifted to the baseband using a quadrature I/Q downconverter. The output signals $x_n^{(I)}(t) = A \cos [2\pi f_c t + 2\pi h \sum_{i=0}^n d_i q(t - iT) + \varphi_0]$ and $x_n^{(Q)}(t) = A \sin [2\pi f_c t + 2\pi h \sum_{i=0}^n d_i q(t - iT) + \varphi_0]$ feed the detection scheme and are transformed in discrete time signals using the CS blocks. Complex vector $\mathbf{y}_n = \mathbf{A}\mathbf{x}_n^{(I)} + j\mathbf{A}\mathbf{x}_n^{(Q)}$ is then used by Algorithm 1 to extract the RSI and to estimate the subcarrier frequency. Finally, the data sequence is derived from the RSI, using the SD scheme implemented by Algorithm 2. To summarize this processing flowchart, the proposed approach is hereafter referred to as SD&CS-RSI. When the RSI is extracted using the FFT instead of the CS, the detection method is referred to as SD&FFT-RSI.

IV. SYSTEM PERFORMANCE

To test the system performance, we simulated an FHSS-GFSK signal in the 2.4-2.48 GHz band, assuming that the synchronization has been already performed by one of the techniques presented in [37, pp. 446–457]. The frequency hopping covers $N_c = 80$ channels of bandwidth $B = 1$ MHz. $N_s = 650$ bits are transmitted during each frequency hop, the subcarrier being pseudo-randomly chosen over the N_c channels. These signal

parameters are typical for the most frequently used drone controllers. An ideal AWGN channel model has been assumed for the transmission of the generated signal, with an E_b/N_0 ratio lying between -5 and 15 dB. For each E_b/N_0 value, 10^4 realizations are considered for the performance evaluation. The CS scheme incorporates m-sequences as kernel functions and consists of L sampling branches, set from 1 to 5 in our simulations. Accordingly, the number of samples per symbol M is varied from 1 to 160 to obtain compression ratios ranging from 1 to 40.

The convergence of the OMP algorithm toward the global optimum is ensured in the noiseless case, for a random \mathbf{W} matrix, provided that [36]

$$LM \geq 2s \log(N_T) \Rightarrow CR \leq \frac{N_T}{2s \log(N_T)}. \quad (12)$$

For instance, $s = 3$ and $N_T = 160$ results in $CR \leq 5$, which justifies the values of the compression ratio considered in our simulations.

The detection performance curves for the compared methods, in terms of BER, are shown in Fig. 9, the feature vectors given by Eq. (10) being calculated from the FFT-extracted and CS-extracted RSI, respectively. Two compression ratios

Algorithm 2 SD of the Data Sequence

Input: RSI matrix $[\hat{\mathbf{X}}_1 \hat{\mathbf{X}}_2 \dots \hat{\mathbf{X}}_{N_s-1}]$, whose columns are obtained using Algorithm 1 from the signals $\{x_n(t)\}_{n=1, \dots, N_s-1}$; centroids $\{\mathbf{P}_i\}_{i=1, \dots, 4}$ corresponding to the couples of data bits $\{1, 1\}$, $\{-1, -1\}$, $\{1, -1\}$, and $\{-1, 1\}$.

Output: Vector of the estimated data bits $\hat{\mathbf{d}} = \{\hat{d}_n\}_{n=0, \dots, N_s-1}$.

- 1: Set $\boldsymbol{\mu} = \mathbf{0}_{N_s-1 \times 1}$, $\boldsymbol{\mu}' = \mathbf{0}_{N_s-1 \times 1}$, $\hat{\mathbf{d}} = \mathbf{0}_{N_s-1 \times 1}$.
- 2: Calculate $\mathbf{p}^{(1)} = \begin{bmatrix} \cos(\arg\{\hat{\mathbf{X}}_1(2)\} - \arg\{\hat{\mathbf{X}}_1(1)\}) \\ \sin(\arg\{\hat{\mathbf{X}}_1(2)\} - \arg\{\hat{\mathbf{X}}_1(3)\}) \end{bmatrix}$.
- 3: Detect the couple $\{d'(i_{\text{opt}}^{(1)}), d''(i_{\text{opt}}^{(1)})\}$ corresponding to $i_{\text{opt}}^{(1)} = \arg \min_{i=1, \dots, 4} \text{dist}\{\mathbf{p}^{(1)}, \mathbf{P}_i\}$.
- 4: Set $\hat{\mathbf{d}}(1) = d'(i_{\text{opt}}^{(1)})$ and $\hat{\mathbf{d}}(2) = d''(i_{\text{opt}}^{(1)})$.
- 5: Calculate $\boldsymbol{\mu}'(1) = 1 - \frac{4 \text{dist}\{\mathbf{p}^{(1)}, \mathbf{P}_i\}}{\sum_{i=1}^4 \text{dist}\{\mathbf{p}^{(1)}, \mathbf{P}_i\}}$ and set $\boldsymbol{\mu}(1) = \boldsymbol{\mu}'(1)$ and $\boldsymbol{\mu}(2) = \boldsymbol{\mu}'(1)$.
- 6: **for** $2 \leq n \leq N_s - 2$ **do**
- 7: Calculate $\mathbf{p}^{(n)} = \begin{bmatrix} \cos(\arg\{\hat{\mathbf{X}}_n(2, n)\} - \arg\{\hat{\mathbf{X}}_n(1, n)\}) \\ \sin(\arg\{\hat{\mathbf{X}}_n(2, n)\} - \arg\{\hat{\mathbf{X}}_n(3, n)\}) \end{bmatrix}$.
- 8: Detect the couple $\{d'(i_{\text{opt}}^{(n)}), d''(i_{\text{opt}}^{(n)})\}$ corresponding to $i_{\text{opt}}^{(n)} = \arg \min_{i=1, \dots, 4} \text{dist}\{\mathbf{p}^{(n)}, \mathbf{P}_i\}$ and set $\hat{\mathbf{d}}(n+1) = d''(i_{\text{opt}}^{(n)})$.
- 9: Calculate $\boldsymbol{\mu}(n) = 1 - \frac{4 \min_{i=1, \dots, 4} \text{dist}\{\mathbf{p}^{(n)}, \mathbf{P}_i\}}{\sum_{i=1}^4 \text{dist}\{\mathbf{p}^{(n)}, \mathbf{P}_i\}}$ and set $\boldsymbol{\mu}(n+1) = \boldsymbol{\mu}'(n)$.
- 10: **if** $\boldsymbol{\mu}'(n) > \boldsymbol{\mu}(n)$ **then**
- 11: Replace the previously estimated $\hat{\mathbf{d}}_n = d''(i_{\text{opt}}^{(n-1)})$ by $\hat{\mathbf{d}}_n = d'(i_{\text{opt}}^{(n)})$.
- 12: Replace the previously calculated $\boldsymbol{\mu}(n) = \boldsymbol{\mu}'(n-1)$ by $\boldsymbol{\mu}(n) = \boldsymbol{\mu}'(n)$.
- 13: **end if**
- 14: **end for**

are considered for the CS scheme: $CR = 1$ ($L = 1, M = 160$) and $CR = 4$ ($L = 4, M = 10$). In the first case, the results provided by the proposed approach (SD&CS-RSI) are similar to those obtained with SD&FFT-RSI and the standard VD. The proposed approach is also compared with an MLP neural network, including one hidden layer with 10 neurons, and trained directly with the RSI. In this case, the feature vector is formed by the concatenation of the real and imaginary parts of the RSI complex components, extracted using the FFT (NNET&FFT-RSI) and the same compressed sampling scheme (NNET&CS-RSI), with $L = 4$ and $M = 10$. The results show that the proposed approach provides a higher detection performance, through the non-linear feature extraction, resulting in better discriminant capabilities. Furthermore, in terms of E_b/N_0 , the performance is improved

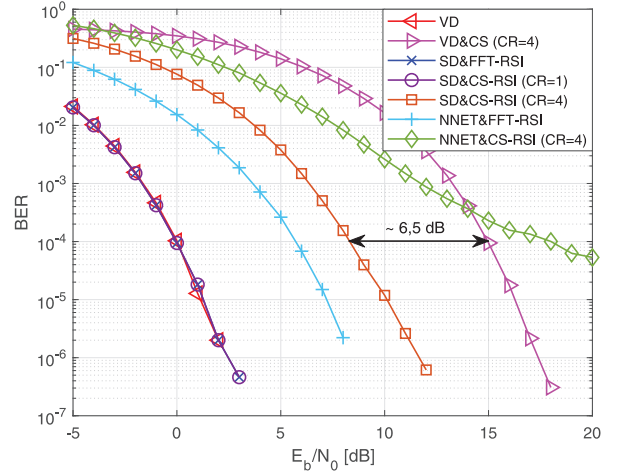


FIGURE 9. Comparison of the FHSS-GFSK detection performance: proposed approach vs. VD- and NNET-based methods.

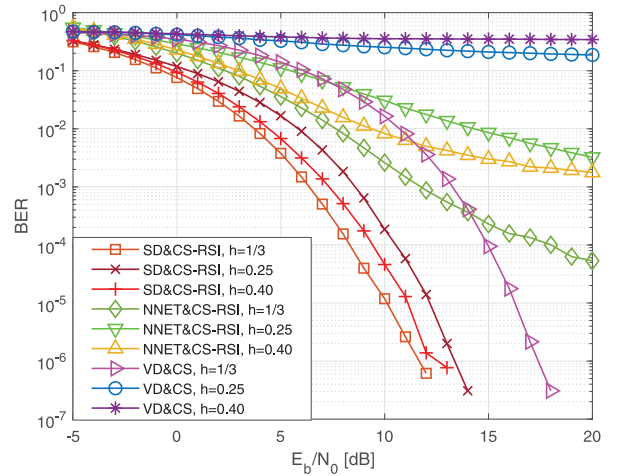


FIGURE 10. Performance sensitivity of the compared detection methods to the variation of modulation index h .

with approximately 6.5 dB at a BER level of 10^{-4} , compared with the reference VD-based approach (VD&CS), for a compression ratio $CR = 4$.

The proposed approach is also much less sensitive to the h value, as shown in Fig. 10. Thus, the BER significantly increases for the NNET-based detector and becomes considerably worse for the VD-based method, whereas for the proposed approach, it gets just slightly lower for a variation of approximately 20% of h around its actual value. To be efficient, the VD-based method requires the right value of modulation index h , and the neural network needs to be trained with data generated using the same h value, which has to be therefore properly estimated.

The proposed approach performance is also plotted in Fig. 11 for different combinations of L and M values, resulting in the same compression ratio $CR = 4$. The BER corresponding to the compression ratio $CR = 1$, obtained for $L = 1$ and $M = 160$, is also added as a reference curve.

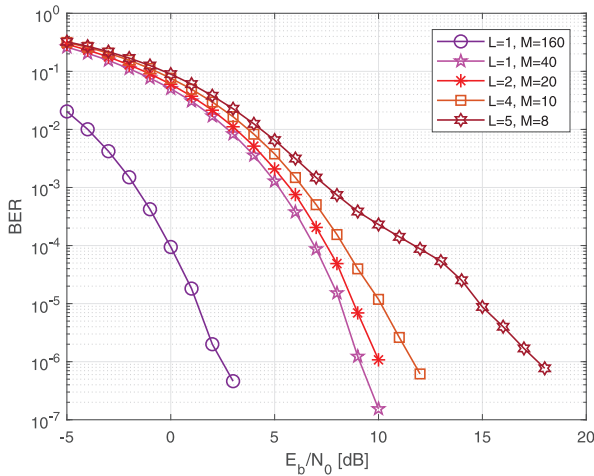


FIGURE 11. SD&CS-RSI performance for different CS parameters.

The detection performance gets slightly lower as the number of CS scheme branches increases, but the BER does not dramatically change for $1 \leq L \leq 5$. However, higher L values enable a more important reduction of the sampling frequency on each CS scheme branch, for a given compression ratio. $L = 4$ is a good trade-off, because the BER is roughly the same as for $L = 1$, and the corresponding value $M = 10$ leads to a sampling frequency 16 times lower than the Nyquist limit. $L = 4$ is a good choice for practical implementations of the CS scheme as well, because larger values of L result in higher complexity hardware, and as the number of channels increases, the impairments related to the electronic devices reduce the system performance.

The same ideal AWGN channel model as in [35] has been assumed so far to compare our results to those provided by the reference method (VD&CS) under the same conditions. When more realistic channel models are considered, the performance of the proposed approach is naturally reduced, as illustrated in Fig. 12. To evaluate the performance loss, two Rayleigh and Rician fading channels are simulated for a maximum Doppler shift of 430 Hz. This value is obtained considering a drone maximum radial speed of 26 m/s [38]. For the Rician channel, a typical K-factor value of 3 is also considered. The measured performance loss, in terms of E_b/N_0 , is more limited for high compression ratios. For $CR = 4$, it is of approximately 2.5 and 11 dB, in the case of the Rician and Rayleigh channels, respectively, at a BER level of 10^{-3} .

Finally, we assessed the complexity of the proposed approach (SD&CS-RSI) and the reference method (VD&CS). Due to the “super-trellis” structure of the reference method decoding scheme, its complexity can be obtained by multiplying with N_c the complexity corresponding to one subchannel carrier frequency. Given the structure of the Viterbi decoder used in [35], its overall complexity for a sequence of N_s compressively sampled ($L \times M$)-length signals can then be expressed as: $O(2LMN_sN_c) = O(2N_TN_sN_c/CR)$. For

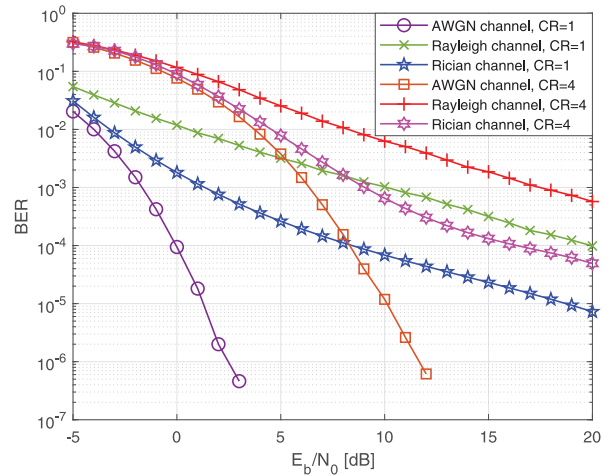


FIGURE 12. Proposed approach performance for different compressive sampling parameters.

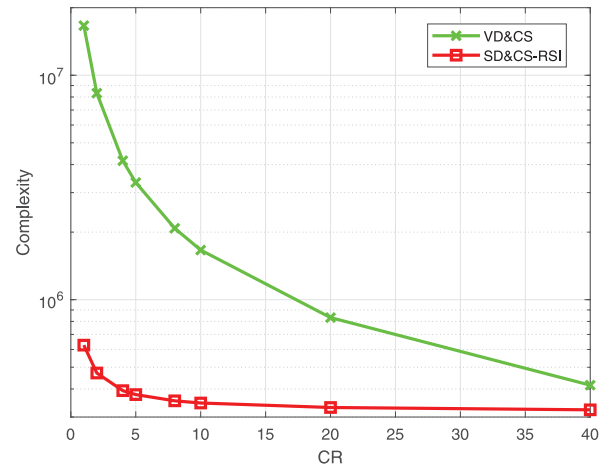


FIGURE 13. Complexity comparison for the proposed approach and the Viterbi based detector.

the proposed approach, we have cumulated the complexities of Algorithms 1 and 2, which are given by $O(3N_s(N_T + ML)) = O(3N_sN_T(CR + 1)/CR)$ [39] and $O(N_s(4m + 1))$, respectively, where $m = 2$ is the dimension of the extracted feature vector in Algorithm 2. Consequently, the overall complexity of the proposed approach is $O(3N_s(N_T(CR + 1)/CR + 3))$. The complexities of the two methods are plotted in Fig. 13 for $N_s = 650$ and $CR \in \{1, 2, 4, 5, 8, 10, 20, 40\}$. The values of the compression ratio are obtained for $N_T = 160$, $L = 4$, and $M \in \{40, 20, 10, 8, 5, 4, 2, 1\}$. The complexity reduction provided by the proposed approach is clearly visible, especially for small to moderate CR . The complexity reduction is actually even more important for our approach since, unlike the reference method, it does not require initial phase estimation.

V. CONCLUSION AND FUTURE WORK

A new detection method for drone control signals has been introduced in this paper. The proposed approach includes

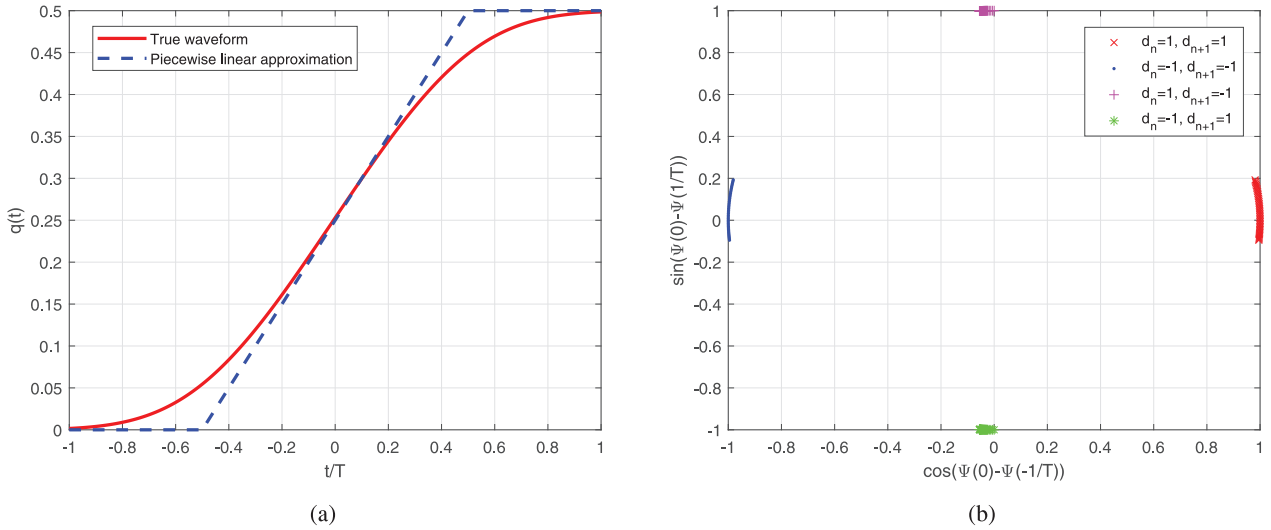


FIGURE 14. Piecewise linear approximation of function $q(t)$ (a) and the corresponding feature vectors distribution for $h \in [0.1, 0.5]$ (b).

retrieving transmitted data bit sequences, coded with the most popular type of modulation used by consumer grade drones, namely FHSS-GFSK. We have thus demonstrated that the pseudo-randomness of the hopping sequence is no longer a barrier that cannot be overcome to access the physical layer, and that this type of communication is resilient to eavesdroppers only to a certain extent. The system is intended to be used in non-cooperative scenarios, where little information about the signals of interest is available. The data bit sequences are recovered by an SD algorithm whose input is a 2D feature vector, derived from the CS-extracted RSI. Counter-drone measures can then be carried out to mislead or take over control of the drone using fake similar signals.

The detection performance of the proposed approach, in terms of BER, is assessed for different compression ratios and compared with that obtained with VD- and NNET-based methods. The proposed approach yields better results in a non-cooperative scenario, while being less sensitive to the variation of the GFSK modulation index. It uses sampling frequencies much lower than the Nyquist limit, does not require the estimation of the signal initial phase, and provides a significant reduction complexity compared with the considered reference method. The detection performance is also evaluated for different CS scheme configurations. The findings show that the detection performance slightly decreases as the number of CS scheme branches increases, but the BER does not dramatically change for $1 \leq L \leq 5$.

The effectiveness of the method described in the paper highlights the fact that current UAV communications are not infallible, and therefore may present some real security issues. Hence, they need to be improved in view of future commercial drone-enabled services. As future work, we plan to proceed with the hardware implementation of the proposed detection approach. The most important technical challenge will be to adapt it to other types of communications and

protocols used by drones, as well as to ensure its satisfactory operation in cluttered environments, where electromagnetic interference can seriously degrade detection performance. Another tricky aspect, after the detection system has been set up, will be to extend the project and implement either a jammer or a spoofer. Finally, if we look beyond the efficiency and functionality aspects of the problem, there will also be challenges related to security policies and legality issues.

APPENDIX

To evaluate the discriminant capability and sensitivity to the modulation index variation of the feature vector defined by Eq. (10), we considered the piecewise linear approximation of function $q(t)$ depicted in Fig. 14(a). It can be readily noticed that

$$\begin{aligned} \theta_2(t) = -\theta_1(t) &\Rightarrow e^{j\theta_2(t)} = \left(e^{j\theta_1(t)} \right)^* \\ \Theta_2(v) = (\Theta_1(-v))^* &\Rightarrow \begin{cases} \psi_{-1,-1}(0) = -\psi_{1,1}(0) \\ \psi_{-1,-1}(-1/T) = -\psi_{1,1}(1/T) \\ \psi_{-1,-1}(1/T) = -\psi_{1,1}(-1/T) \end{cases} \\ \theta_4(t) = -\theta_3(t) &\Rightarrow e^{j\theta_4(t)} = \left(e^{j\theta_3(t)} \right)^* \\ \Theta_4(v) = (\Theta_3(-v))^* &\Rightarrow \begin{cases} \psi_{-1,1}(0) = -\psi_{1,-1}(0) \\ \psi_{-1,1}(-1/T) = -\psi_{1,-1}(1/T) \\ \psi_{-1,1}(1/T) = -\psi_{1,-1}(-1/T) \end{cases} \end{aligned}$$

Hence,

$$\begin{aligned} \mathbf{P}_2 &= \begin{bmatrix} \cos(\psi_{-1,-1}(0) - \psi_{-1,-1}(-1/T)) \\ \sin(\psi_{-1,-1}(0) - \psi_{-1,-1}(1/T)) \end{bmatrix} \\ &= \begin{bmatrix} \cos(\psi_{1,1}(0) - \psi_{1,1}(1/T)) \\ -\sin(\psi_{1,1}(0) - \psi_{1,1}(-1/T)) \end{bmatrix} \\ \mathbf{P}_4 &= \begin{bmatrix} \cos(\psi_{-1,1}(0) - \psi_{-1,1}(-1/T)) \\ \sin(\psi_{-1,1}(0) - \psi_{-1,1}(1/T)) \end{bmatrix} \\ &= \begin{bmatrix} \cos(\psi_{1,-1}(0) - \psi_{1,-1}(1/T)) \\ -\sin(\psi_{1,-1}(0) - \psi_{1,-1}(-1/T)) \end{bmatrix} \end{aligned}$$

Fourier transforms $\Theta_1(\nu)$ and $\Theta_3(\nu)$ are then calculated using the Wolfram Mathematica software and the resulting phases for $\nu \in \{-1/T, 0, 1/T\}$ as a function of the index modulation h are given below:

$$\begin{cases} \psi_{1,1}(-1/T) = 2\pi h + \pi \\ \psi_{1,1}(0) = -\frac{\pi}{2} - \arctan\left[\frac{8\text{sinc}(\pi h)\cos(2\pi h)}{8\text{sinc}(\pi h)\sin(2\pi h)+1}\right] \\ \psi_{1,1}(1/T) = 2\pi h \end{cases}$$

and

$$\begin{cases} \psi_{1,-1}(-1/T) = \pi h + \pi \\ \psi_{1,-1}(0) = \arctan\left[\frac{\text{sinc}(\pi h)\sin(2\pi h)}{\text{sinc}(\pi h)\cos(2\pi h)-1}\right] \\ \psi_{1,-1}(1/T) = \pi h + \pi \end{cases}$$

Consequently,

$$\begin{aligned} \mathbf{P}_2 &= \begin{bmatrix} \cos(\psi_{1,1}(0) - \psi_{1,1}(-1/T) + \pi) \\ -\sin(\psi_{1,1}(0) - \psi_{1,1}(1/T) - \pi) \end{bmatrix} \\ &= \begin{bmatrix} -\cos(\psi_{1,1}(0) - \psi_{1,1}(-1/T)) \\ \sin(\psi_{1,1}(0) - \psi_{1,1}(1/T)) \end{bmatrix} \end{aligned}$$

and

$$\mathbf{P}_4 = \begin{bmatrix} \cos(\psi_{1,-1}(0) - \psi_{1,-1}(-1/T)) \\ -\sin(\psi_{1,-1}(0) - \psi_{1,-1}(1/T)) \end{bmatrix}.$$

Thus, we finally obtain:

$$\begin{aligned} \mathbf{P}_1 &= \begin{bmatrix} \cos(\psi_{1,1}(0) - \psi_{1,1}(-1/T)) \\ \sin(\psi_{1,1}(0) - \psi_{1,1}(1/T)) \end{bmatrix}, \\ \mathbf{P}_2 &= \begin{bmatrix} -\cos(\psi_{1,1}(0) - \psi_{1,1}(-1/T)) \\ \sin(\psi_{1,1}(0) - \psi_{1,1}(1/T)) \end{bmatrix}, \\ \mathbf{P}_3 &= \begin{bmatrix} \cos(\psi_{1,-1}(0) - \psi_{1,-1}(-1/T)) \\ \sin(\psi_{1,-1}(0) - \psi_{1,-1}(1/T)) \end{bmatrix}, \\ \mathbf{P}_4 &= \begin{bmatrix} \cos(\psi_{1,-1}(0) - \psi_{1,-1}(-1/T)) \\ -\sin(\psi_{1,-1}(0) - \psi_{1,-1}(1/T)) \end{bmatrix}. \end{aligned}$$

The expressions derived above demonstrate the discriminant characteristic of the proposed feature vector, as they correspond to well-separated points within the unit square. Indeed, the first and second components of \mathbf{P}_1 and \mathbf{P}_2 are opposite and identical, respectively, whereas for \mathbf{P}_3 and \mathbf{P}_4 , they are identical and opposite, respectively. Thus, \mathbf{P}_1 and \mathbf{P}_2 , as well as \mathbf{P}_3 and \mathbf{P}_4 , are symmetric with respect to the origin along the horizontal axis and vertical axis, respectively.

The distribution of the feature vectors when the GFSK modulation index h varies between 0.1 and 0.5 is shown in Fig. 14(b). It confirms the conclusion that we have already drawn on the basis of the results plotted in Fig. 10, i.e., the weak sensitivity of the proposed feature vector to the variation of the modulation index.

REFERENCES

- [1] *Dedrone*. Accessed: Jan. 18, 2020. [Online]. Available: <https://www.dedrone.com/resources/incidents/all>
- [2] Research and Markets. (2019). *The Drone Market Report 2019: Commercial Drone Market Size and Forecast (2019–2024)*. Accessed: Oct. 12, 2019. [Online]. Available: <https://www.researchandmarkets.com/reports/4764173/the-drone-market-report-2019-commercial-drone>
- [3] G. C. Birch, J. C. Griffin, and M. K. Erdman, *UAS Detection, Classification, and Neutralization: Market Survey*, Sandia Nat. Lab., Albuquerque, NM, USA, 2015.
- [4] D. Lee, W. G. La, and H. Kim, “Drone detection and identification system using artificial intelligence,” in *Proc. Int. Conf. Inf. Commun. Technol. Converg. (ICTC)*, Oct. 2018, pp. 1131–1133.
- [5] A. Rozantsev, V. Lepetit, and P. Fua, “Detecting flying objects using a single moving camera,” *IEEE Trans. Pattern Anal. Mach. Intell.*, vol. 39, no. 5, p. 1, May 2017.
- [6] K. Stasiak, M. Ciesielski, A. Kurowska, and W. Przybysz, “A study on using different kinds of continuous-wave radars operating in C-band for drone detection,” in *Proc. 22nd Int. Microw. Radar Conf. (MIKON)*, May 2018, pp. 521–526.
- [7] M. Jian, Z. Lu, and V. C. Chen, “Drone detection and tracking based on phase-interferometric doppler radar,” in *Proc. IEEE Radar Conf. (RadarConf)*, Apr. 2018, pp. 1146–1149.
- [8] J. Drozdowicz *et al.*, “35 GHz FMCW drone detection system,” in *Proc. 17th Int. Radar Symp. (IRS)*, May 2016, pp. 1–4.
- [9] M. Z. Anwar, Z. Kaleem, and A. Jamalipour, “Machine learning inspired sound-based amateur drone detection for public safety applications,” *IEEE Trans. Veh. Technol.*, vol. 68, no. 3, pp. 2526–2534, Mar. 2019.
- [10] I. Djurek, A. Petosic, S. Grubesa, and M. Suhanek, “Analysis of a quadcopter’s acoustic signature in different flight regimes,” *IEEE Access*, vol. 8, pp. 10662–10670, 2020.
- [11] I. Bisio, C. Garibotto, F. Lavagetto, A. Sciarrone, and S. Zappatore, “Blind detection: Advanced techniques for WiFi-based drone surveillance,” *IEEE Trans. Veh. Technol.*, vol. 68, no. 1, pp. 938–946, Jan. 2019.
- [12] P. Nguyen *et al.*, “Towards RF-based localization of a drone and its controller,” in *Proc. 5th Workshop Micro Aerial Veh. Netw. Syst. Appl. (DroNet)*, Jun. 2019, pp. 21–26.
- [13] M. Haluza and J. Cechak, “Analysis and decoding of radio signals for remote control of drones,” in *Proc. New Trends Signal Process. (NTSP)*, Oct. 2016, pp. 1–5.
- [14] Y. Zeng, Q. Wu, and R. Zhang, “Accessing from the sky: A tutorial on UAV communications for 5G and beyond,” *Proc. IEEE*, vol. 107, no. 12, pp. 2327–2375, Dec. 2019.
- [15] *IEEE 802.11TM Wireless Local Area Networks*. Accessed: Oct. 12, 2019. [Online]. Available: <http://www.ieee802.org/11/>
- [16] D. Mototolea, “A study on the actual and upcoming drone communication systems,” in *Proc. Int. Symp. Signals Circuits Syst. (ISSCS)*, Jul. 2019, pp. 1–4.
- [17] G. de Goeij, E. H. van Dijken, and F. Brouwer, *Research Into the Radio Interference Risks of Drone*, Strict B.V., Utrecht, Netherlands, May 2016. Accessed: Mar. 19, 2019. [Online]. Available: <https://www.agentschaptelecom.nl/documenten/rapporten/2017/december/6/rapport-research-into-the-radio-interference-risks-of-drones>
- [18] J. G. Proakis, *Digital Communications*, 4th ed. New York, NY, USA: McGraw-Hill, 2000.
- [19] F. Xiong, *Digital Modulation Techniques*. Norwood, MA, USA: Artech House, 2006.
- [20] L. Sun and Q. Du, “A review of physical layer security techniques for Internet of Things: Challenges and solutions,” *Entropy*, vol. 20, p. 730, Sep. 2018.
- [21] X. Sun, D. W. K. Ng, Z. Ding, Y. Xu, and Z. Zhong, “Physical layer security in UAV systems: Challenges and opportunities,” *IEEE Wireless Commun.*, vol. 26, no. 5, pp. 40–47, Oct. 2019.
- [22] Q. Wu, W. Mei, and R. Zhang, “Safeguarding wireless network with UAVs: A physical layer security perspective,” *IEEE Wireless Commun.*, vol. 26, no. 5, pp. 12–18, Oct. 2019.
- [23] I. Harjula, J. Pinola, and J. Prokkola, “Performance of IEEE 802.11 based WLAN devices under various jamming signals,” in *Proc. Mil. Commun. Conf. (MILCOM)*, Nov. 2011, pp. 2129–2135.
- [24] H. Shin, K. Choi, Y. Park, J. Choi, and Y. Kim, “Security analysis of FHSS-type drone controller,” in *Proc. Revised Sel. Papers 16th Int. Workshop Inf. Security Appl. (WISA)*, Jeju Island, South Korea, vol. 9503, 2015, pp. 240–253.
- [25] K. Parlin, M. M. Alam, and Y. Le Moullec, “Jamming of UAV remote control systems using software defined radio,” in *Proc. Int. Conf. Mil. Commun. Inf. Syst. (ICMCIS)*, May 2018, pp. 1–6.

- [26] K. Haeng-Bok, J.-S. Lee, and E.-R. Jeong, "Analysis of frequency hopping signals in commercial drones," *Int. J. Pure Appl. Math.*, vol. 118, no. 19, pp. 2015–2024, 2018.
- [27] C. Zhong, J. Yao, and J. Xu, "Secure UAV communication with cooperative jamming and trajectory control," *IEEE Commun. Lett.*, vol. 23, no. 2, pp. 286–289, Feb. 2019.
- [28] E. J. Candes and M. B. Wakin, "An introduction to compressive sampling," *IEEE Signal Process. Mag.*, vol. 25, no. 2, pp. 21–30, Mar. 2008.
- [29] E. J. Candes, J. Romberg, and T. Tao, "Robust uncertainty principles: Exact signal reconstruction from highly incomplete frequency information," *IEEE Trans. Inf. Theory*, vol. 52, no. 2, pp. 489–509, Feb. 2006.
- [30] D. L. Donoho, "Compressed sensing," *IEEE Trans. Inf. Theory*, vol. 52, no. 4, pp. 1289–1306, Apr. 2006.
- [31] E. J. Candes and T. Tao, "Near-optimal signal recovery from random projections: Universal encoding strategies?" *IEEE Trans. Inf. Theory*, vol. 52, no. 12, pp. 5406–5425, Dec. 2006.
- [32] J. Yuan, P. Tian, and H. Yu, "The detection of frequency hopping signal using compressive sensing," in *Proc. Int. Conf. Inf. Eng. Comput. Sci.*, Dec. 2009, pp. 1–4.
- [33] F. Liu, M. W. Marcellin, N. A. Goodman, and A. Bilgin, "Compressive sampling for detection of frequency-hopping spread spectrum signals," *IEEE Trans. Signal Process.*, vol. 64, no. 21, pp. 5513–5524, Nov. 2016.
- [34] J. Wu, N. Liu, Y. Zhang, and C. Shen, "Blind detection of frequency hopping signal based on compressive sensing," in *Proc. 2nd Int. Conf. Consum. Electron. Commun. Netw. (CECNet)*, Apr. 2012, pp. 1691–1694.
- [35] L. Pan, M. W. Marcellin, W. E. Ryan, and B. Vasic, "Viterbi detection for compressively sampled FHSS-GFSK signals," *IEEE Trans. Signal Process.*, vol. 63, no. 22, pp. 5965–5975, Nov. 2015.
- [36] G. Kutyniok and Y. C. Eldar, *Compressed Sensing*. Cambridge, U.K.: Cambridge Univ. Press, 2013.
- [37] R. Poisel, *Modern Communications Jamming Principles and Techniques*, 2nd ed. Norwood, MA, USA: Artech, 2011.
- [38] *Droneversus*. Accessed: Jan. 21, 2020. [Online]. Available: <https://droneversus.com/speed>
- [39] B. L. Sturm and M. G. Christensen, "Comparison of orthogonal matching pursuit implementations," in *Proc. 20th Eur. Signal Process. Conf. (EUSIPCO)*, Aug. 2012, pp. 220–224.